ORIGINAL ARTICLE

3D iteratively reconstructed spatial resolution map and sensitivity characterization of a dedicated cardiac SPECT camera

John A. Kennedy, PhD,[a] Ora Israel, MD,[a,b] and Alex Frenkel, PhD[a]

[a] Department of Nuclear Medicine, Rambam Health Care Campus, P.O. Box 9602, Haifa, Israel
[b] B. and R. Rappaport School of Medicine, Technion, Israel Institute of Technology, Haifa, Israel

Background. A solid-state cadmium zinc telluride (CZT) SPECT device provides ultrafast myocardial perfusion imaging (MPI) with a spherical field-of-view (FOV). This study aims at determining the spatial resolution and sensitivity throughout this FOV as a guide for patient positioning.

Methods and Results. For this CZT camera (Discovery 570c, GE Healthcare), the iteratively reconstructed spatial resolution along 3 Cartesian axes was compared (average resolution 6.9 ± 1.0 mm full-width at half-maximum) using a 2 dimensional array of point sources in air which was aligned with a transverse plane shifted throughout the FOV. Sensitivity was plotted in the central transverse slice and axially in locations comparable to the placement of the heart in 266 rest/stress cardiac studies (M 78, age 63 ± 13 years). The average sensitivity was 0.46 ± 0.19 kc/s/MBq with a transverse gradient of 0.039 ± 0.001 kc/s/MBq/cm (8.9% of the sensitivity per cm). Reconstructed relative activity was uniform (uniformity <9%) and count rate was linear ($R = 0.999$) over 3 orders of magnitude.

Conclusions. The CZT SPECT camera offers good resolution, sensitivity, and uniformity, and provides linearity in count rate. A gradient of >8%/cm in sensitivity justifies the crucial role of patient positioning with the heart closest to the detector. (J Nucl Cardiol 2014;21:443–52.)

Key Words: Myocardial perfusion imaging: SPECT · instrumentation: SPECT · ultrafast cardiac gamma camera · cadmium-zinc-telluride

INTRODUCTION

Radionuclide myocardial perfusion imaging (MPI) has been an essential diagnostic tool for the assessment of known or suspected coronary artery disease (CAD) for more than 20 years.[1,2] Recently there is an increasing interest in the use of dedicated cardiac cameras for MPI.[3] Dedicated cardiac solid-state cadmium zinc telluride (CZT) cameras offer ultrafast MPI. These cameras have the potential of drastically reducing the administered radiotracer dose and thus radiation exposure or, alternatively, to decrease the acquisition time to as low as 2 minutes[4,5] and thus minimize motion artifacts and increase patient comfort and throughput.[3,6] Furthermore, reducing the administered dose is a very timely issue since future supplies of ^{99}Mo/^{99m}Tc are uncertain and expected to be limited.[7] Clinical trials have shown images obtained with these systems to be comparable to dual head Anger cameras using either filtered back-projection[8] or iterative[9,10] reconstruction. Simultaneous ultrafast acquisition of all tomographic projections facilitate the implementation of optimized clinical protocols such as dynamic studies that will allow measurements of coronary flow reserve.[11-13]

For this study, the Discovery NM 570c (DNMC, GE Healthcare, Tirat HaCarmel, Israel) was the cardiac solid state camera characterized. The DNMC, offering a unique design, has been introduced in recent years[14]

444   J. A. Kennedy et al.
Characterization of a cardiac SPECT camera

Journal of Nuclear Cardiology®
May/June 2014

and to the best of our knowledge the spatial dependence of performance measurements such as spatial resolution and sensitivity has not been detailed in peer-reviewed publications so far. Although dedicated cardiac CZT cameras have been characterized by National Electrical Manufacturers Association (NEMA)-like tests[15-17] the static L-shaped layout of the detector panels of DNMC suggests that the field-of-view (FOV) of this focused pinhole system is unlikely to have the cylindrical symmetry for which some of these measures have been designed. Consequently the objective of this study was to provide a characterization of the unique FOV, concerning mainly parameters relevant to optimal patient positioning for clinical image acquisition.

MATERIALS AND METHODS

Cardiac CZT System

The system consists of 19 solid-state CZT detectors with a multi-pinhole collimator each giving projection data in a 32×32 matrix with 2.46 mm × 2.46 mm pixels. The detector is physically pixelated defining a projection bin size of 1 pixel. During acquisition, the detectors are stationary and acquire data simultaneously, supporting reconstruction on a 19-cm diameter spherical FOV. The approximate geometric relationship among the detectors and pinholes has been published,[18] and these positions are shown with respect to the FOV in Fig. 1. The camera has been used for a more than fivefold shortening of MPI scan times[4] and its design is described in detail elsewhere.[16] This study design included measuring the iteratively reconstructed spatial resolution throughout the FOV, the spatial resolution of the projection data, measuring the sensitivity, uniformity with respect to relative reconstructed values, and count rate.

Spatial Resolution

To develop a volumetric spatial resolution map, a phantom consisting of an array of 30 point sources in air set in a transverse plane in a 5 cm × 5 cm grid (Fig. 2). The point sources were made from capillary tubes, 1 mm in diameter, each with a drop of ~ 1.5 MBq ^{99m}Tc pertechnetate less than 1.5-mm long, and set in a polystyrene foam block. The phantom was stepped axially by 2.5 cm throughout the FOV and 2 minute acquisition performed at each step. The phantom was also shifted such that locations every 2.5 cm in the 2 transverse orthogonal directions were sampled for a total of 36 acquisitions. Using an Xeleris workstation (GE Healthcare, Tirat HaCarmel, Israel), images were reconstructed with the manufacturer's proprietary 3D maximum likelihood expectation maximization (MLEM) algorithm which modeled system geometry including collimator response compensation.[16] Projection data were summed before reconstruction such that planes of point sources separated by 5 cm axially were
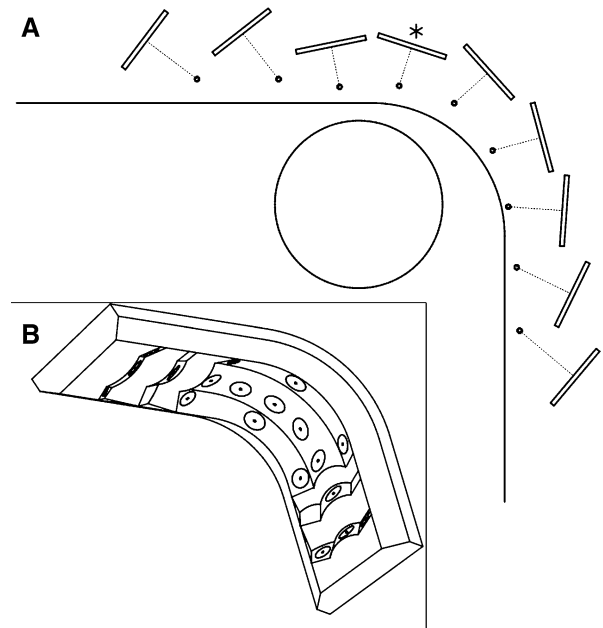

Figure 1. Approximate geometry of the CZT detectors (*rectangles*) and pinholes (*small circles*) in relation to the detector cover (*L-shape*). (**A**) The 9 detectors located in the central transverse plane are shown. The 19-cm diameter supported reconstruction region (*large circle*) is centered approximately 11 cm from the anterior face and 16 cm from the left lateral face of the detector cover. The raw data spatial resolution was measured for the detector marked with the asterisk. (**B**) The 3D relationship of the 19 pinholes depicted as ellipses on the detector face.

Figure 2. To map spatial resolution in air, 30 point sources were arrayed in a 5-cm grid pattern set in a polystyrene foam block, as shown here, and stepped throughout the camera FOV in 2.5-cm increments. Patient left corresponds to the *left side* of this image.

reconstructed simultaneously. The default reconstruction for clinical imaging comprises 40 iterations with regularization, a 70 × 70 matrix, a 4-mm voxel size, and Butterworth post-filtering (order 7, cutoff frequency 0.37). Images were reconstructed using the default reconstruction but without post-filtering.

The reconstructed spatial resolution was calculated by means of a semi-automatic measurement of the full-width at half-maximum (FWHM) along the 3 orthogonal axes: lateral (left/right), vertical (dorsal/ventral), and axial (superior/inferior). The FWHM precision was limited by the 4 mm reconstructed voxel size determined by the system matrix. In transverse views, the approximate locations of the sources were chosen manually. In house software was developed that searched the neighborhood of each chosen point to determine the voxel with the maximum signal for that point and each FWHM was calculated based on a parabolic fit including adjacent voxels. A stack of 50 4 mm thick transverse image slices spanned 20 cm axially. Maximum intensity projections of the spatial resolution results through the 14 central transverse planes (the axial center ±2.8 cm) onto a common transverse plane, provided the FWHM measurements from which the interpolated spatial resolution maps were calculated. Values for unsampled pixels were estimated by bi-linear interpolation. A fourth ''worst case'' map was constructed by choosing the maximal values from the transverse maps for the 3 orthogonal directions. Reslicing the image space provided 70 4-mm thick coronal slices spanning 28 cm in the dorsal/ventral direction. Similar coronal maps were made using 14 coronal central planes.

In addition, the raw spatial resolution acquired in the projection data was measured for one of the detectors (marked in Fig. 1). A 2 MBq ^{99m}Tc pertechnetate source restricted to a 1-mm diameter capillary tube and <1 mm in length was placed in front of the pinhole at distances ranging from 5 to 21 cm from the pinhole. This required the removal of the detector cover to expose the pinhole location. A similar source was placed lateral to the first source to provide a measurement to determine the minification/magnification of the pinhole. In the projection data, the FWHM and peak positions were determined by linear interpolation. The raw data spatial resolution was taken as the FWHM of the first source.

Sensitivity

A 2D map of the absolute sensitivity in the FOV for the axially central transverse slice was obtained by placing a single 8-mm sphere of approximately 37 MBq of ^{99m}Tc pertechnetate in a 3 cm × 3 cm grid on a 7 × 7 matrix pattern throughout the FOV and performing repeated 1 minute acquisitions. A plexiglass mounting bracket held flush to the end of an empty Jaszczak phantom (Data Spectrum Corp., Hillsborough NC, USA) cylinder was used as a jig (Fig. 3). Absolute sensitivities were calculated from the projection data as the total counts in one minute divided by the decay corrected activity for 64 sampled points in 51 locations in the central transverse plane and assigned to the maximum pixel for that acquisition. Beyond the quality FOV, the sensitivity measurement was

discarded if the projection data were truncated. Within the FOV, additional acquisitions were used to double-check previously sampled locations leading to 13 twice-sampled pixels. This method was repeated for the central coronal slice, but no additional acquisitions in the FOV were performed. To plot the 2D sensitivity maps, unsampled pixels were estimated by bi-linear interpolation. Eight of the locations sampled for the transverse sensitivity map were chosen for plotting additional absolute sensitivity measurements along the axial direction by translating the jig in 1 cm steps across the 20 cm length of the detector heads (Fig. 3). No account was made for any small attenuation provided by the plexiglass.

To evaluate the relative sensitivity in the reconstructed images, the counts from reconstructed image of each sensitivity measurement were summed and corrected for activity and decay. In the transverse and coronal planes, the uniformity (U) among these points was calculated as:

$$U = (C_{max} - C_{min})/(C_{max} + C_{min}) \qquad (1)$$

where C_{max} was the total counts from the image with the maximum counts and C_{min} was the corresponding result from the image with the minimum counts.

The sensitivity map was compared to the placement of the heart in the scanner using a retrospective analysis of 266 clinical studies. Approval for this study was received from the Helsinki committee of our institution. These were same day rest/stress studies following the injection of 370 MBq ^{99m}Tc-sestimibi at rest and 1110 MBq at stress in 133 consecutive patients: age 63.6 ± 13.0 years, including 78 males and 55 females, body mass index (BMI) 28.8 ± 4.9 kg/m^2, height 167 ± 9 cm, weight 80 ± 15 kg, with a likelihood of CAD defined as low ($n = 20$), medium ($n = 73$), and high ($n = 40$). As a rule, patient positioning with the myocardium centered in

Figure 3. Throughout the axially central transverse plane, 64 sensitivity measurements were made. Additional axial sensitivity plots were made for eight transverse locations and are shown here with respect to the detector face. The locations are referred to in the text as ''nearest'' (*black circle*), ''top'' (*white circle*), ''center'' (*red circle*), ''bottom'' (*orange circle*), ''top right'' (*yellow circle*), ''right'' (*green circle*), ''bottom right'' (*blue circle*), and ''left'' (*violet circle*). In this figure only, patient left corresponds to the left side of the image.

446   J. A. Kennedy et al.
Characterization of a cardiac SPECT camera

Journal of Nuclear Cardiology®
May/June 2014

the FOV was accomplished in under 1 minute with the aid of the manufacturer's real-time display of projections from 3 of the detectors in the anterior, left-lateral, and oblique anterior/left-lateral positions. To visually compare the clinical placement of the heart with respect to the sensitivity map, the approximate edge of the myocardial wall of each study was defined as 40% the maximum value found within the myocardial wall and drawn as a contour for the central transverse and coronal slices overlaid with the positions of the sensitivity measurements. The contours of the average images were also drawn for the central transverse and coronal slices. In addition, each myocardial wall was inspected to determine if it fell entirely within the spherical FOV without truncation.

Count Rate

The count rate performance test was performed as per the manufacturer's recommended method (MRM) using 2 mL of ^{99m}Tc pertechnetate in a sealed syringe with an activity 1.01 GBq, placed in the centre of the FOV and was further allowed to decay until the system was no longer saturated and the system software enabled the acquisition. Five 1 minute acquisitions were performed over a 12-hour duration. Since in MRM just a small portion of each detector is activated and has little scatter, an additional count rate test was performed using a 6.5-L featureless Jaszczak phantom cylinder that filled the entire FOV using an activity of 1.35 GBq of ^{99m}Tc pertechnetate. Data were acquired 7 times over a 58-hour duration. Acquisition times varied from 10 seconds to 40 minutes to keep the total counts within the same order of magnitude. Count rates in the energy window used for ^{99m}Tc-sestimibi cardiac SPECT acquisitions (140.5 keV ±10%) were plotted against the incident count rate[16] and the results were analyzed for a linear relationship.

RESULTS

For measurement of spatial resolution in air, in the entire acquisition space 212/466 imaged point sources (51%) fell within the 19-cm diameter spherical quality FOV. Iteratively reconstructed spatial resolution maps were interpolated from 123 points from the 14 central transverse slices (Fig. 4) and 123 points from 14 central coronal slices (Fig. 5). The average iteratively reconstructed spatial resolution is given in Table 1 and for the portion of the maps falling within 13 cm of the L-shaped detector cover (approximating the quadrant closest to the detectors), the average resolution was 10% better than the resolution throughout the FOV. The raw spatial resolution of one of the detectors is shown in Figure 6 as a function of source distance from the pinhole. For this detector, a distance of 14 cm from the pinhole corresponded to the center of the FOV.

For the transverse sensitivity map, most of the contours delineating the myocardial wall fell within the region covered by the sampled points (Fig. 7A). The

placement of the left ventricle was entirely within the FOV in 96% (256/266) of the studies. The measured sensitivity ranged from 0.91 kc/s/MBq near the elbow of the L-shaped detector cover to 0.20 kc/s/MBq in the region of the FOV farthest from the detectors (Fig. 7B). The average sensitivity in the FOV for the central transverse slice was 0.46 ± 0.19 kc/s/MBq as calculated from the interpolated sensitivity map. For the example left ventricle myocardium delineated in Figure 7, the sensitivity was estimated to vary from 0.31 to 0.66 kcps/MBq. The sensitivity decreased as the point source was moved axially to the edge of the detectors (Fig. 8) with the largest changes in sensitivity occurring in the position nearest to the detectors at the superior edge.

Uniformity was 6.2% and 8.1% among the reconstructed acquisitions for the central transverse and central coronal planes, respectively.

The maximum count rate for MRM was 418 kc/s and a linear fit of observed vs incident count rate (Fig. 9) gave residuals of −0.59% to 0.7% with an R value (correlation coefficient) of 0.999. The corresponding values for the 6.5 L source were a maximum count rate of 192 kc/s, residuals of −2.3% to 2.8%, and an R value of 0.999. This linearity was observed over 3 orders of magnitude, down to a count rate of 0.253 kc/s.

DISCUSSION

The iteratively reconstructed spatial resolution maps are not smoothly varying from pixel to pixel (Fig. 4) which may be, in part, due to the sample spacing set by the limited pixel size versus the resolution or by not having an optimal projection bin size. The average spatial resolution of 6.9 ± 1.0 mm is consistent with the value of 6.7 mm reported elsewhere,[17] although the comparison is limited because of different methods. For example, to facilitate 3D mapping, point sources were used in this study instead of line sources. Overall, 3D iteratively reconstructed spatial resolution maps show that the resolution as measured by the point sources in air remains below 10 mm FWHM except for the lateral resolution at the dorsal side of the FOV and for the vertical resolution at the right hand side of the FOV, the 2 regions farthest from the detector cover. Therefore, positioning the heart as close as possible to the detectors insures the best resolution. Regions of higher spatial resolution within the sub-volume encompassing the heart will lead to better contrast, a more accurate depiction of small lesions, and more accurate quantitation in cardiac regions closest to the detector because of reduced partial volume effects. The map of the iteratively-reconstructed spatial resolution in the axial direction shows better inter-slice separation in regions closest to the detectors (Figures 4C and 5C).
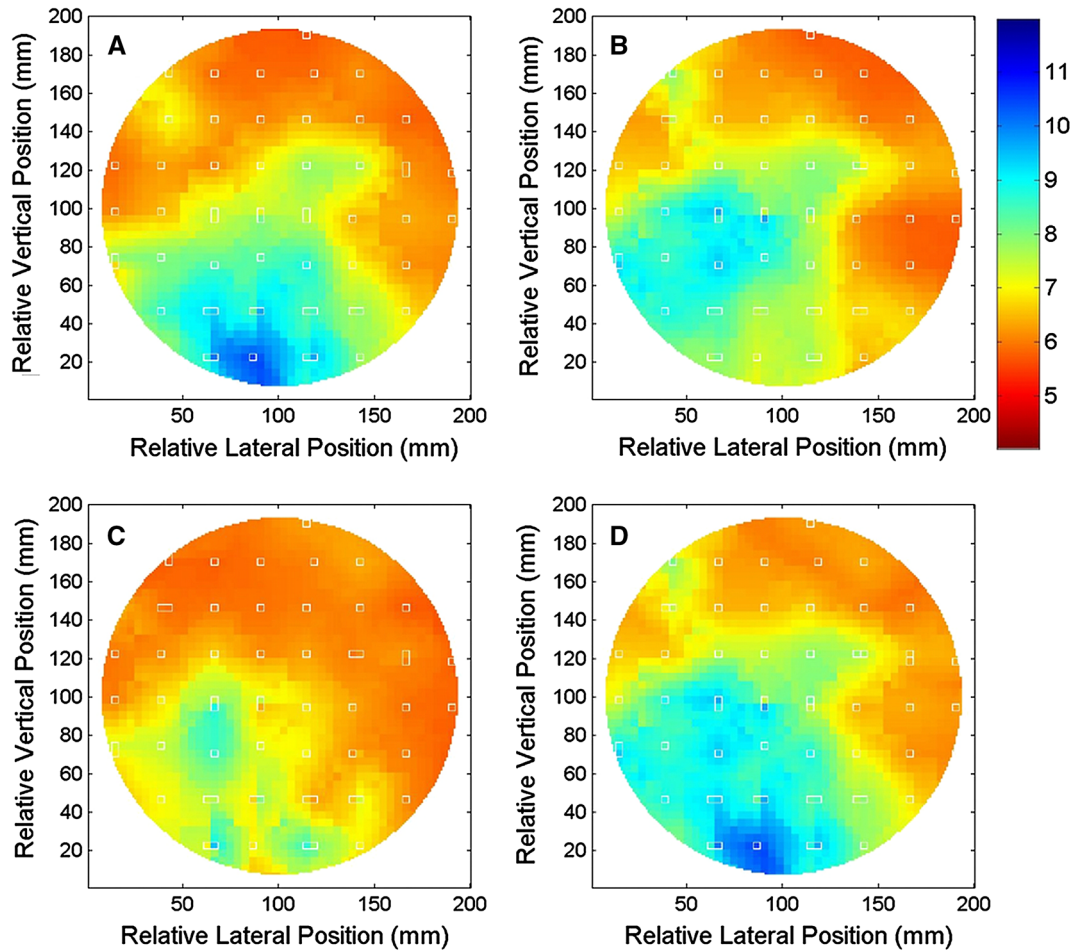
Figure 4. Transverse maps of iteratively reconstructed spatial resolution as measured by point sources in air with default reconstruction parameters in the three orthogonal directions: lateral (**A**), vertical (**B**), axial (**C**), and maximal value of all three maps (**D**). Maps were interpolated from 123 points from the 14 central transverse slices. The values are given in mm FWHM. Sampled points are marked by *white borders*.

The default clinical reconstruction parameters provided a reasonable limit to the number of MLEM iterations applied to the point sources in air, since clinical reconstructions with these parameters have been shown to provide MPI images comparable to standard dual detector cameras.[9] Establishing a limit is necessary since if an arbitrarily large number of MLEM iterations is chosen, the point sources in air will tend to be reconstructed into single voxels, giving artificially small FWHM measurements for point sources in air.[19,20] Since DNMC geometry precludes the application of filtered backprojection reconstruction used in the NEMA performance standards NU 2-2001,[21] this study was limited to evaluating only the iteratively reconstructed results throughout the FOV which do not correspond directly to the spatial resolution in such standards. The measurements provide an indication of spatial variation in resolution, but underestimate the resolution obtained using clinical reconstruction parameters and post-filtering. However, comparisons within the FOV or among similar cameras remain certain.

The spatial resolution (R_{total}) of a pinhole in planar projection data is

$$R_{total} = \sqrt{d^2(1 + 1/M)^2 + R_{det}^2/M^2} \qquad (2)$$

where d is the effective pinhole diameter, M is the magnification/minification, and R_{det} is the intrinsic detector resolution. Near the pinhole, M is very large and the spatial resolution is approximately equal to the effective pinhole diameter. A linear extrapolation of spatial resolution measurements in Fig. 6 gives an estimate of 4.9 ± 0.5 mm at the pinhole, which is in agreement with the 4.95 mm estimate previously published for the effective pinhole diameter.[18]

448   J. A. Kennedy et al.
        Characterization of a cardiac SPECT camera

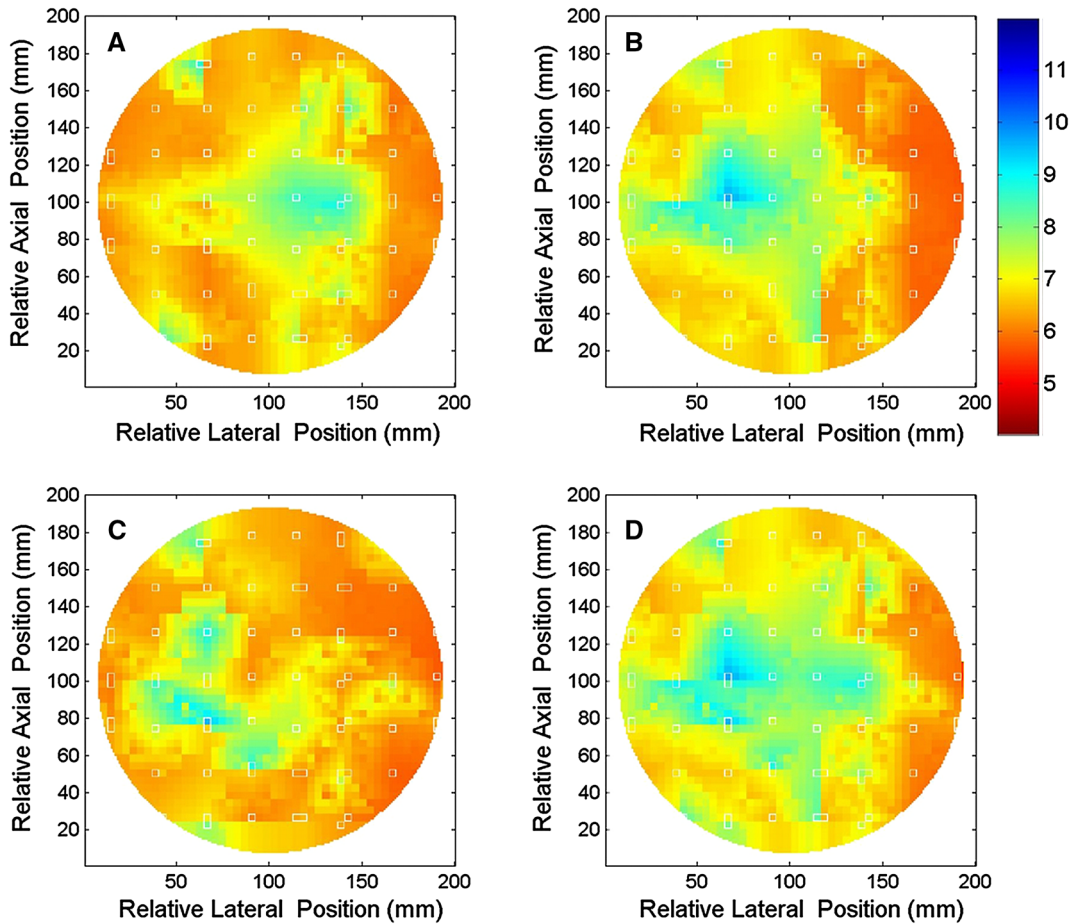Journal of Nuclear Cardiology®
May/June 2014

Figure 5. Coronal maps of iteratively reconstructed spatial resolution as measured by point sources in air with default reconstruction parameters in the three orthogonal directions: lateral (**A**), vertical (**B**), axial (**C**), and maximal value of all three maps (**D**). Maps were interpolated from 123 points from the 14 central coronal slices. The values are given in mm FWHM. Sampled points are marked by *white borders*.

Table 1. Iteratively reconstructed spatial resolution map measurements

| Directions | Point sources in air | |
	Entire FOV FWHM (mm)	Within 13 cm of detectors FWHM (mm)
Lateral	7.1 ± 1.1	6.4 ± 0.5
Vertical	7.1 ± 1.0	6.3 ± 0.6
Axial	6.5 ± 0.7	6.1 ± 0.2
Average	6.9 ± 1.0	6.2 ± 0.5

The plots of sensitivity along the axial direction show that the sensitivity peaks near the center of the axial FOV (Fig. 8). The heart should be placed as a rule at a location where the sensitivity is greatest. Although this occurs closest to the detectors, the axial gradients are larger at this location as compared to those for locations farther from the detector. The spatial variation in sensitivity throughout the FOV must be compensated for in the reconstruction. Present results indicate that the sensitivity plots in the axial direction are not varying smoothly and this is most likely caused by the asymmetrical nature of the jig holding the sources.
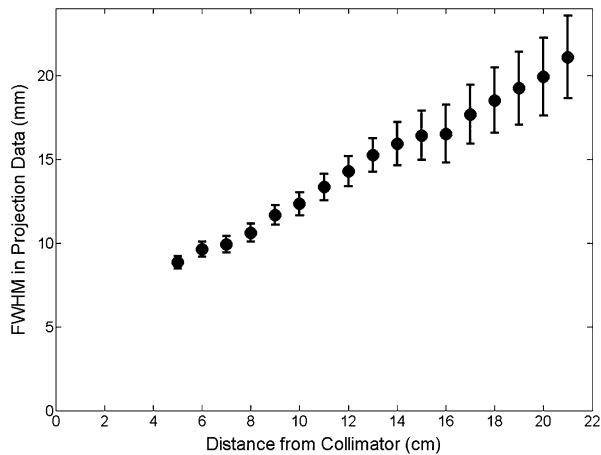
Figure 6. Spatial resolution of the projection data as measured by the FWHM of a ^{99m}Tc source in air <1 mm in diameter as a function of distance from the pinhole collimator of one detector.

Measurements in the superior locations were reduced by the small attenuation provided by the plexiglass cylinder. Consequently, the peaks appear shifted to the inferior side of the 100-mm axial center mark. Also, the discrete nature of overlapping FOVs for each pinhole likely caused the non-smooth variability in the sensitivity as the jig moved axially through each FOV.

The gradients of the 2D sensitivity map passing through the center of the FOV were found heuristically to have an inverse exponential relationship with distance. For the maximum gradient, found at 29.0° from the normal to the upper detector, the fit ($R = 0.999$, residuals <4.5%) could be described as:

$$s = 0.84 \exp(-0.089x) \tag{3}$$

where s is sensitivity, and x is distance from the edge of the FOV in cm, giving a gradient of 8.9 ± 0.1%/cm (average: 0.039 ± 0.001 kc/s/MBq/cm). The in/out movement of the detector heads as defined by the gantry is along the 45° angle. A similar fit ($R = 0.999$, residuals <1.9%) along this angle gives an expected gain in sensitivity of 8.5% for every cm the detector is moved in toward the heart for a given patient and, because of the log-linear relationship, this holds true regardless whether the heart is positioned close to or far from the detector.

With respect to the sensitivity maps (Fig. 7), the placement of the heart in clinical studies was good, with 255 of 266 studies completely within the FOV. The sensitivity measurements in this study are higher than values typically reported for dual detector cameras configured for MPI,[3,22,23] but this difference in sensitivity may not directly reflect the variation in the image noise, since with iterative reconstruction with resolution

modeling, as in DNMC, there is a trade-off between the resolution and the reconstructed noise. High sensitivity can be achieved for MPI with conventional cameras fitted with special collimators[24] and conventional camera geometries do not yield an increase in sensitivity for CZT.[25] However, compact CZT detectors provide for flexibility in design allowing for a better compromise between resolution and sensitivity for an organ-specific FOV than might be obtained with non-pixilated detectors.

The count rate linearity in the clinical range (average 3.3 ± 1.0 kc/s for rest, 14.3 ± 4.8 kc/s for stress, range of 1.3-32.0 kc/s) was demonstrated by the larger phantom with scatter but not MRM (Fig. 9). Beyond the manufacturer's recommendations, the MRM would need to be extended for an additional 42 hour to sample count rates down to the clinical ranges or to be repeated with smaller activities. The lower maximum count rate for the larger phantom was due to scatter. There is no traditional event pile-up loss with this camera. Due to limitations within the digital circuitry, no events are processed beyond the maximum count rate and the count rate will remain linear up to this threshold.

DNMC employs only 19 projections and has a small FOV. Although increased angular sampling would likely improve image quality,[24] DNMC performs well with respect to the diagnostic accuracy for MPI studies[9] and for relative quantitation tasks.[16] Uniformity among the reconstructed images of small sources was good (<9%), indicating good compensation for variations in sensitivity during reconstruction, but not all the points in the FOV could be practically sampled by this method. Standard phantoms do not fit the spherical FOV, so are subject to truncation artifacts. A spherical uniformity phantom of appropriate size has given an integral uniformity of 12%, but Chang attenuation correction is typically applied before uniformity measurements and this remains commercially unavailable with DNMC.[26] In cardiac phantom scans, DNMC gives good uniformity and good contrast with cold lesions.[16] However, because of the limited FOV and angular sampling, it cannot be used for large, complicated organs such as the brain.

Only non-attenuation corrected results were evaluated for the present study. Since by far the majority of these cameras are installed without CT, the aim was to characterize the SPECT camera. For DNMC, CT attenuation correction (CTAC) reduces the number of attenuation artifacts in clinical studies[27] and the value of CTAC is greater for larger patients.[28] Consequently, further characterization with attenuating media and CTAC would be worthwhile. Additional prone imaging can reveal if apparent reduced uptake in the inferior myocardial wall during supine imaging is an attenuation
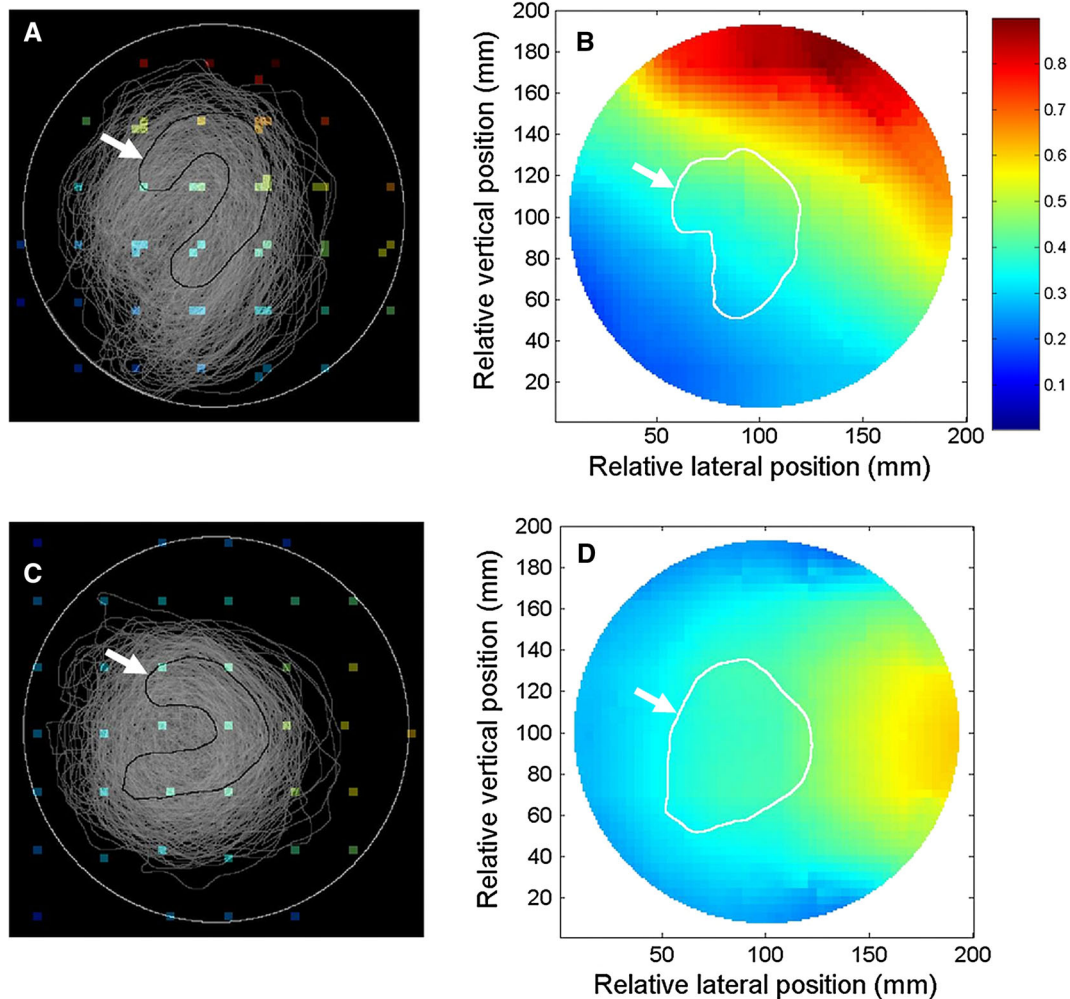
450 J. A. Kennedy et al.
Characterization of a cardiac SPECT camera

Journal of Nuclear Cardiology®
May/June 2014

Figure 7. Sensitivity measurements in the central transverse slice. (**A**) Plot of location of 64 measurements overlaid onto the log-intensity *gray scale* image of the myocardial contours of 266 clinical acquisitions. The *white circle* denotes the limit of the supported reconstruction region. *Arrow* denotes an example contour in black. (**B**) An interpolated map of the sensitivity in kc/s/MBq. *Arrow* denotes the contour of the average of all acquisitions. (**C**) and (**D**) corresponding coronal images based on 39 measurements.

artifact and this method has been applied successfully using CZT cameras.[29]

The characteristics of the FOV of the DNMC need to be considered when positioning patients. Truncation of the heart data in the projection images may cause artifacts.[24] Placing the left ventricle consistently in the center of the limited FOV of DNMC is required to reduce the possibility of truncation, however challenging in patients with larger thoracic size. Placing the heart in the axial center ensures maximum sensitivity and reduces the chance of truncation at the superior or inferior ends. Initial studies under typical clinical conditions do not indicate that truncation of projection data from background and other organs, such as the liver, adversely affect clinical image quality[9,16] although the magnitude of these effects should be investigated in the future. Also worthy of investigation is the positioning of obese patients. Although the camera has been shown to perform well in detecting CAD for a non-obese population with short scan times of <5 minutes,[30] it becomes difficult to obtain diagnostic image quality for a very obese population.[28] In addition, positioning the heart as close as possible to the elbow of the L-shaped detector cover ensures the best iteratively reconstructed spatial resolution with subsequent substantially superior sensitivity. In MPI studies performed with DNMC it is imperative therefore, to locate the heart in an axially central location as close as possible to the two detector faces.
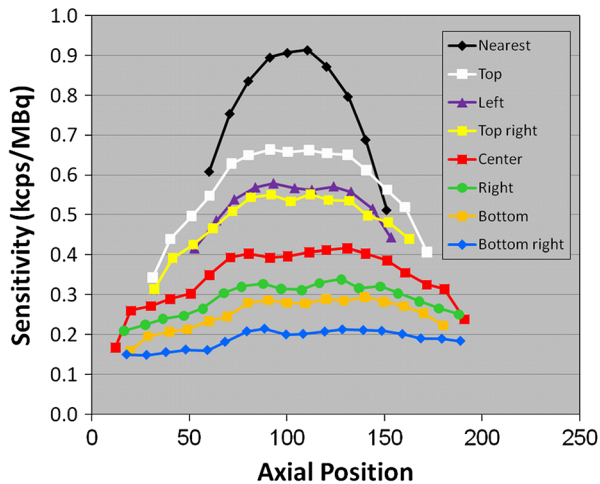
Figure 8. Axial plot of sensitivity from the superior end of the detector. The holder for the source had low attenuation but was axially asymmetrical. The higher sensitivities are from axial plots closer to the detectors (Fig. 3).
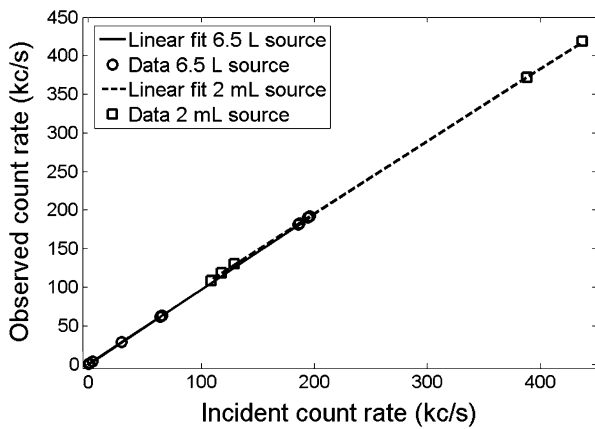

Figure 9. The plot of system observed count rate as a function of the incident count rate for the ^{99m}Tc energy window (140.5 keV ±10%). The larger source provides more scatter out of this window giving a lower maximum count rate. The relationship is linear over three orders of magnitude.

NEW KNOWLEDGE GAINED

For an ultrafast cardiac CZT SPECT camera both the spatial resolution and the sensitivity vary throughout the FOV such that they are best in the region closest to the elbow of the L-shaped detector cover. Patient positioning with the heart closest to the detector has a crucial role justified by a gradient in sensitivity of more than 8%/cm.

CONCLUSION

The best average iteratively reconstructed spatial resolution of the DNMC was found within 13 cm of the detector with a value of 6.2 mm FWHM as measured by a point source array in air and was spatially variant throughout the FOV. The average sensitivity was 0.46 kc/s/MBq. The uniformity was good and the count rate was linear. Patient positioning with the heart closest to the detector has a crucial role justified by a gradient in sensitivity of more than 8%/cm.

References

1. Hendel RC, Berman DS, Di Carli MF, Heidenreich PA, Henkin RE, Pellikka PA, et al. ACCF/ASNC/ACR/AHA/ASE/SCCT/SCMR/SNM 2009 Appropriate Use Criteria for Cardiac Radionuclide Imaging. J Am Coll Cardiol 2009;53:2201-29.
2. Hendel RC, Abbott BG, Bateman TM, Blankstein R, Calnon DA, Leppo JA, et al. ASNC Information Statement: The Role of Radionuclide Myocardial Perfusion Imaging for Asymptomatic Individuals. J Nucl Cardiol 2011;18:3-15.
3. Slomka PJ, Patton JA, Berman DS, Germano G. Advances in Technical Aspects of Myocardial Perfusion SPECT Imaging. J Nucl Cardiol 2009;16:255-76.
4. Herzog BA, Buechel RR, Katz R, Brueckner M, Husmann L, Burger IA, et al. Nuclear Myocardial Perfusion Imaging with a Cadmium-Zinc-Telluride Detector Technique: Optimized Protocol for Scan Time Reduction. J Nucl Med 2010;51:46-51.
5. Gambhir SS, Berman DS, Ziffer J, Nagler M, Sandler M, Patton J, et al. A Novel High-Sensitivity Rapid-Acquisition Single-Photon Cardiac Imaging Camera. J Nucl Med 2009;50:635-43.
6. Schillaci O, Danieli R. Dedicated Cardiac Cameras: a New Option for Nuclear Myocardial Perfusion Imaging. Eur J Nucl Med Mol Imaging 2010;37:1706-9.
7. Organisation for Economic Co-Operation and Development, Nuclear Energy Agency. The Supply of Medical Radioisotopes Implementation of the HLG-MR Policy Approach: Results from a Self-Assessment by the Global 99Mo/99mTc Supply Chain. The Supply of Medical Radioisotopes series 2013. http://www.oecd-nea.org/med-radio/med-radio-series.html.
8. Sharir T, Ben-Haim S, Merzon K, Prochorov V, Dickman D, Ben-Haim S, et al. High-Speed Myocardial Perfusion Imaging Initial Clinical Comparison with Conventional Dual Detector Anger Camera Imaging. J Am Coll Cardiol Imaging 2008;1:156-63.
9. Esteves FP, Raggi P, Folks RD, Keidar Z, Wells Askew J, Rispler S, et al. Novel Solid-State-Detector Dedicated Cardiac Camera for Fast Myocardial Perfusion Imaging: Multicenter Comparison with Standard Dual Detector Cameras. J Nucl Cardiol 2009;16:927-34.

452 J. A. Kennedy et al.
Characterization of a cardiac SPECT camera

Journal of Nuclear Cardiology®
May/June 2014

10. Buechel RR, Herzog BA, Husmann L, Burger IA, Pazhenkottil AP, Treyer V, et al. Ultrafast Nuclear Myocardial Perfusion Imaging on a New Gamma Camera with Semiconductor Detector Technique: First Clinical Validation. Eur J Nucl Med Mol Imaging 2010;37:773-8.

11. Sharir T, Slomka PJ, Berman DS. Solid-State SPECT Technology: Fast and Furious. J Nucl Cardiol 2010;17:890-6.

12. Gullberg GT, Reutter BW, Sitek A, Maltz JS, Budinger TF. Dynamic Single Photon Emission Computed Tomography—Basic Principles and Cardiac Applications. Phys Med Biol 2010;55:R111-91.

13. Ben-Haim S, Murthy VL, Breault C, Allie R, Sitek A, Roth N, et al. Quantification of Myocardial Perfusion Reserve Using Dynamic SPECT Imaging in Humans: A Feasibility Study. J Nucl Med 2013;54:873-9.

14. Garcia EV, Faber TL. Advances in Nuclear Cardiology Instrumentation: Clinical Potential of SPECT and PET. Curr Cardiovasc Imaging Rep 2009;2:230-7.

15. Erlandsson K, Kacperski K, van Gramberg D, Hutton BF. Performance Evaluation of D-SPECT: a Novel SPECT System for Nuclear Cardiology. Phys Med Biol 2009;54:2635-49.

16. Bocher M, Blevis IM, Tsukerman L, Shrem Y, Kovalski G, Volokh L. A Fast Cardiac Gamma Camera with Dynamic SPECT Capabilities: Design, System Validation and Future Potential. Eur J Nucl Med Mol Imaging 2010;37:1887-902.

17. Imbert L, Poussier S, Franken PR, Songy B, Verger A, Morel O, Wolf D, Noel A, Karcher G, Marie P-Y. Compared Performance of High-Sensitivity Cameras Dedicated to Myocardial Perfusion SPECT: A Comprehensive Analysis of Phantom and Human Images. J Nucl Med 2012;53:1897-903.

18. Jansen FP, Tsukerman L, Volokh L, Blevis I, Hugg JW, Bouhnik JP. Uniformity Correction Using Non-uniform Floods. Conf Rec IEEE Nuclear Sci Symp Medical Imaging Conf 2010;1:2314-8.

19. Snyder DL, Miller MI. The Use of Sieves to Stabilize Images Produced with the EM Algorithm for Emission Tomography. IEEE Trans Nucl Sci 1985;32:3864-72.

20. Miller TR, Walhis JW. Clinically Important Characteristics of Maximum Likelihood Reconstruction. J Nucl Med 1992;33:1678-84.

21. National Electrical Manufacturers Association. Performance Measurements of Gamma Cameras. NEMA Standards Publication NU 1-2007. Rosslyn, VA: National Electrical Manufacturers Association; 2007.

22. Patton J, Sandler M, Berman D, Vallabhajosula S, Dickman D, Gambhir S, et al. D-SPECT: A New Solid State Camera for High Speed Molecular Imaging. (Abstract). J Nucl Med 2006;47(suppl 1):189P.

23. Fleming JS, Alaamer AS. Influence of Collimator Characteristics on Quantification in SPECT. J Nucl Med 1996;37:1832-6.

24. Funk T, Kirch DL, Koss JE, Botvinick E, Hasegawa BH. A Novel Approach to Multipinhole SPECT for Myocardial Perfusion Imaging. J Nucl Med 2006;47:595-602.

25. Amrami R, Shani G, Hefetz Y, Blevis I, Pansky A. A comparison between the performance of a pixellated CdZnTe based gamma camera and Anger NaI(Tl) scintillator gamma camera. Engineering in Medicine and Biology Society, 2000. Proceedings of the 22nd Annual International Conference of the IEEE; 2000. p 352-5.

26. Hillel P, Hanney M, Redgate S, Taylor J, Randall D. Assessing the Performance of a Solid-State Cardiac Gamma Camera Prior to Its Introduction into Routine Clinical Service. J Nucl Med 2011;52(Supplement 1):1937.

27. Herzog BA, Buechel RR, Husmann L, Pazhenkottil AP, Burger IA, Wolfrum M, et al. Validation of CT Attenuation Correction for High-Speed Myocardial Perfusion Imaging Using a Novel Cadmium-Zinc-Telluride Detector Technique. J Nucl Med 2010;53:1539-44.

28. Fiechter M, Gebhard C, Fuchs TA, Ghadri JR, Stehli J, Kazakauskaite E, et al. Cadmium-Zinc-Telluride Myocardial Perfusion Imaging in Obese Patients. J Nucl Med 2012;53:1401-6.

29. Piszczek S, Dziuk M, Gizewska-Krasowska A, Mazurek A. Inferior Wall Attenuation Artifact on CZT Gamma Camera. Is Prone Imaging Better Than Stand-Alone CT Attenuation Correction (CTAC)? Eur J Nucl Med Mol Imaging 2013;40(Suppl 2):S463.

30. Duvall WL, Sweeny JM, Croft LB, Ginsberg E, Guma KA, Henzlova MJ. Reduced Stress Dose with Rapid Acquisition CZT SPECT MPI in a Non-obese Clinical Population: Comparison to Coronary Angiography. J Nucl Cardiol 2012;19:19-27.